Inductively Coupled Plasma Mass Spectrometer with Axial Field in a Quadrupole Reaction Cell

Dmitry R. Bandura, Vladimir I. Baranov, and Scott D. Tanner
PerkinElmer-SCIEX, Concord, Ontario, Canada

A novel reaction cell for ICP-MS with an electric field provided inside the quadrupole along its axis is described. The field is implemented via a DC bias applied to additional auxiliary electrodes inserted between the rods of the quadrupole. The field reduces the settling time of the pressurized quadrupole when its mass bandpass is dynamically tuned. It also improves the transmission of analyte ions. It is shown that for the pressurized cell with the field activated, the recovery time for a change in quadrupole operating parameters is reduced to <4 ms, which allows fast tuning of the mass bandpass in concert with and at the speed of the analyzing quadrupole. When the cell is operated with ammonia, the field reduces ion-ammonia cluster formation, further enhancing the transmission of atomic ions that have a high cluster formation rate. $Ni{\cdot}(NH3)_n^+$ cluster formation in a cell operated with a wide bandpass (i.e., Ni^+ precursors are stable in the cell) is shown to be dependent on the axial field strength. Clusters at n = 2–4 can be suppressed by 9, 1200, and >610 times, respectively. The use of a retarding axial field for in-situ energy discrimination against cluster and polyatomic ions is shown. When the cell is pressurized with O_2 for suppression of $^{129}Xe^+$, the formation of $^{127}IH_2^+$ by reactions with gas impurities limits the detection of ^{129}I to isotopic abundance of $\sim 10^{-6}$. In-cell energy discrimination against $^{127}IH_2^+$ utilizing a retarding axial field is shown to reduce the abundance of the background at m/z = 129 to ca. 3×10^{-8} of the $^{127}I^+$ signal. In-cell energy discrimination against $^{127}IH_2^+$ is shown to cause less I^+ loss than a post-cell potential energy barrier for the same degree of $^{127}IH_2^+$ suppression. (J Am Soc Mass Spectrom 2002, 13, 1176–1185) © 2002 American Society for Mass Spectrometry

Ion-molecule reactions are routinely used in ICP-MS for reduction of isobaric spectral interferences [1–11]. Appropriate selection of a reaction gas can provide very efficient reactive suppression of Ar-containing interfering ions keeping analyte losses small [12]. An example of a typical ion-molecule reactor is an rf-driven multipole ion guide, which is encapsulated (gas-tight housing, entrance and exit apertures) and pressurized with a reaction gas. The most efficient utilization of this technique includes the quadrupole with adjustable mass bandpass dynamic reaction cell (DRC) [12–15]. The topic of this investigation is related to an important modification of this device and the experimental verification of some fundamental principles of its operation.

Inside an ion-molecule reactor, the flux of reactive ions diminishes according to its reactivity and the number density of the neutral molecule, producing an equivalent amount of product ions. The product ions usually have different masses and reactivity and might react further. Use of the quadrupole inside the reactor allows operating the ion reactor with a mass bandpass that has well-defined boundaries of stability. Quick, efficient, and selective rejection of unwanted ions is thus made possible. Selection of the appropriate bandpass minimizes formation of new "in cell" interferences by rejection of their precursors and can provide many orders of magnitude (10^5–10^8) improvements of signal-to-background for ICP-MS detection of Ca^+, K^+, Fe^+, As^+, Se^+, V^+, and other usually interfered analytes [15, 16].

However, in some interesting cases the bandpass should include the product ions. For example, oxidation or fluorination of analyte ions with N_2O, O_2, or CH_3F to quantify them as oxides or fluorides has been shown to be useful [1, 17, 18].

Ions that do not react with the reaction gas experience multiple collisions, which can cause collisional focusing towards the cell axis and thus better transmission through the exit aperture [19]. Concurrently, radial velocity and displacement of some ions after some collisions can fall outside the ellipse of acceptance of the quadrupole, causing scattering losses. The net effect on transmission depends on the ion-neutral mass ratio,

Published online August 22, 2002
This article presented in part at the January, 2002 Winter Conference on Plasma Spectrochemistry, Scottsdale, Arizona.
Address reprint requests to Dr. D. R. Bandura, Research Department, MDS SCIEX, 71 Four Valley Drive, Concord, Ontario L4K 4V8, Canada. E-mail: dmitry.bandura@sciex.com

1044-0305/02/$20.00
PII S1044-0305(02)00435-X
Received March 12, 2002
Revised May 8, 2002
Accepted June 19, 2002

energy of the ions, confining rf-field, and gas pressure [19]. Many useful ion-molecule reactions have ion–reaction gas mass ratios close to unity, such that scattering losses are significant. In addition, a relatively high number of collisions (i.e., high gas pressure) is favorable for attenuation of strong interferences, further exacerbating transmission or scattering losses.

It has been shown [20] that ion kinetic energy is reduced by collisions with the reaction gas and that ion transit time through the pressurized quadrupole is increased by at least an order of magnitude (to few milliseconds) compared to a nonpressurized device. This effect has found important application in the measuring of isotope ratios due to the associated temporal homogenization of the ion flux. In addition, Hattendorf and Günter observed that a significant (ca. 500 ms) settling time is required for the ion signals to reach steady-state levels after a large change (ca. from $m/z = 13$ to $m/z = 132$) of the low mass cut-off of the pressurized quadrupole cell. The effect was attributed to a significant increase in ion residence time [21].

Increased ion transit time was also observed in triple quadrupole mass spectrometers that had been pressurized to a relatively high pressure (few mTorr) inside the collision cell. In this instance, the increased ion transit time caused hysteresis effects during precursor ion scans [22]. This occurs because the pressurized cell traps the previous parent ion and its fragments for a time period longer than the scanning time of the first mass-selecting quadrupole. An effective means of mitigating this increased ion transit time is to establish an axial field inside the cell that directs the ions toward the cell exit between collisions [23, 24]. A convenient design for providing such an axial field that also retains the bandpass characteristics of a quadrupole was recently suggested by Loboda et al. [25].

We present here the results of investigations of the transient and other characteristics of the pressurized quadrupole reaction cell and the effects of the axial field on the ion transit time, scattering losses, settling time, cluster ion formation, and transport of polyatomic ions produced in the cell.

Experimental

Experiments were performed using a research prototype of the instrument (ELAN DRC) that has been described in detail elsewhere [13]. It was equipped with a reaction cell of modified geometry that accommodated additional electrodes inserted between the quadrupole rods. The additional electrodes were connected and biased to the same potential V_{AFT}. The ion optics drive was also modified to study the effect of the axial field on ion residence time by introducing an optionally pulsed ion beam into the pressurized cell, in a manner similar to that described in [20]. In these studies the entrance aperture of the cell was biased independently to the exit aperture of the cell. The bias voltages are denominated as V_{CE} (cell entrance) and V_{CP} (cell exit, or cell path). Other voltages applied are V_{CRO} (DC potential common to all four rods of the cell) and V_{QRO} (DC potential common to all four rods of the analyzing quadrupole). To obtain ion pulses from the continuous ion beam, the autolens was pulsed from +20 V (ions repelled) to +8 V (optimum for $^{107}Ag^+$ ions) for the duration of 2 ms at 1 Hz frequency using an HP 33120A Arbitrary Waveform Generator (Hewlett-Packard Company, Loveland, CO). Ion signals from the pulse stage of the dual-stage detector were recorded with a Multichannel Scaler (model SR430, Stanford Research Systems, Stanford, CA).

Samples were prepared from 1000 μg/mL PE Pure single-element standard solutions (PerkinElmer, Shelton, CT) by sequential dilution with high purity deionised water (DIW) produced using an Elix/Gradient (Millipore, Bedford, MA) water purification system and acidified using ultrapure Nitric Acid (Baseline, Seastar Chemicals, Sidney, BC, Canada).

Stock solution of iodine (1000 mg/kg) was prepared from I_2 flakes (I37-100, Fisher Scientific, Nepeon, ON, Canada) by dissolving in 100% isopropyl alcohol (GIGABIT, Ashland Chemical, Dublin, OH).

Ammonia (99.9995%) and oxygen (99.998%) reaction gases from Matheson Gas products (Whitby, Canada) were used. Ammonia was introduced through the internal getter of the instrument, and an additional oxygen purifying getter (NuPure Model 40, NuPure Corp., Ottawa, Canada) was used for oxygen. Gas flows were controlled by mass flow controllers (MKS Instruments, Methuen, MA) calibrated for Ar; thus all gas flow units (unless stated otherwise) are given in Ar-equivalent s.c.c.m. units set in the instrument control software. The coefficients for the unit conversion to s.c.c.m. for a particular gas can be found elsewhere [37].

Axial Field Implementation

The field was provided by additional auxiliary electrodes inserted between the quadrupole rods in a manner similar to that described in [25]. An external DC power supply (Model 205A-05R, Bertan Associates Inc., Syosset, NY) was used for biasing the electrodes to a positive (for accelerating field) or a negative (for retarding field) DC potential.

The electric potential on the axis is defined by the potentials of the quadrupole rods and auxiliary electrodes. As the distance between the edge of the auxiliary electrodes and the axis of the quadrupole varies along the axis, so does the DC potential, and thus a potential gradient is established along the axis. SIMION 3D (version 7.00, Idaho National Engineering and Environmental Laboratory, Idaho Falls, ID) modeling of a static quadrupole with the geometry of the DRC, with shaped auxiliary electrodes inserted between the rods, shows that for 300 V DC applied to the auxiliary electrodes, a homogeneous field of ca. 33.3 V/m is established along the axis. The field along the line 2 (Figure 1) which is parallel to the axis but 2 mm closer

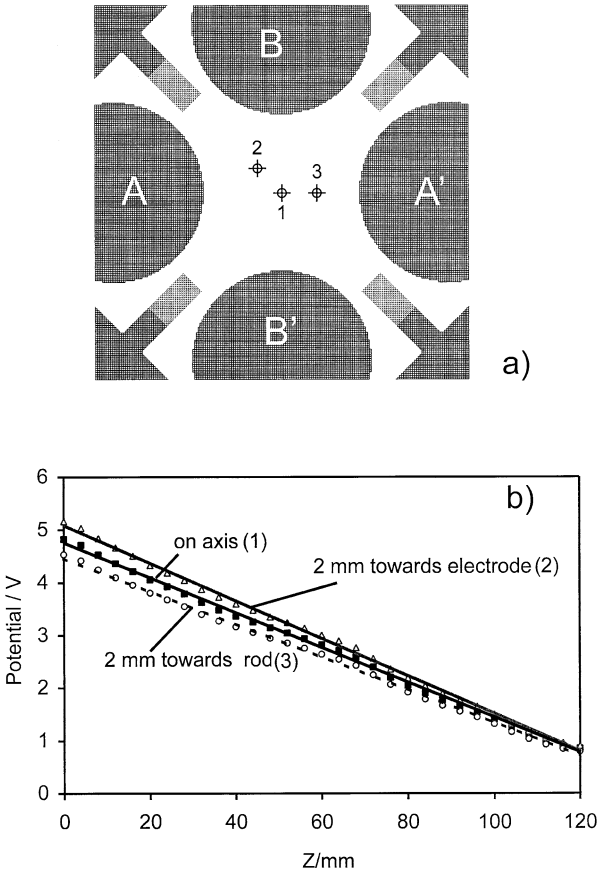

Figure 1. Simion 3-D model cross-section (**a**) and d.c. potential dependence along the z-axis obtained by the modeling at V_{AFT} = 300 V (**b**). Potential distributions were calculated along principal axis (1) and two lines parallel to the principal axis and positioned 2 mm off towards one of the auxiliary electrodes (2) or towards one of the quadrupole rods (3).

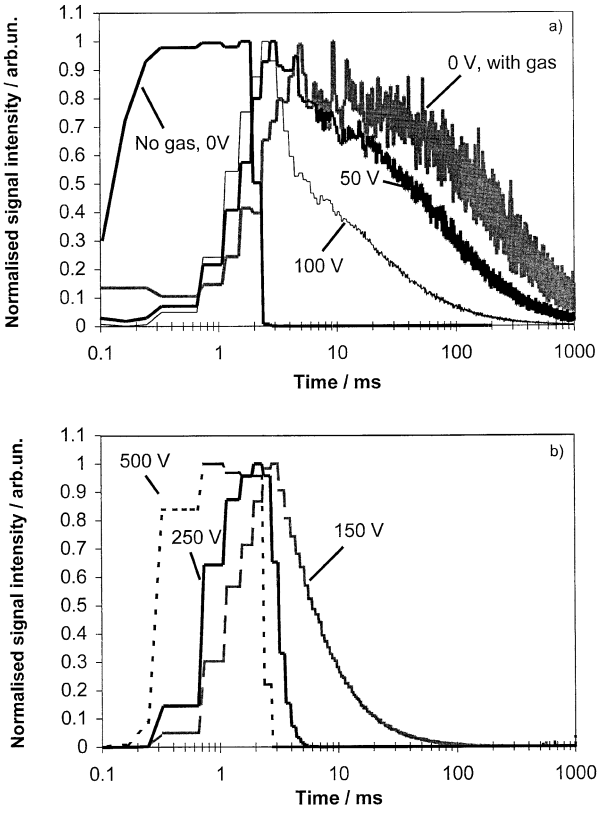

Figure 2. Arrival time distributions for $^{107}Ag^+$ ion pulse of 2 ms duration for the cell pressurized with Ne at different V_{AFT}.

to the auxiliary electrode is somewhat stronger (35.6 V/m), while that along the line 3 (Figure 1), which is 2 mm closer to the quadrupole rod, is somewhat weaker (31.3 V/m). Thus, the difference in the axial field strength within a cross-section of 4 mm diameter is less than ±7% from the field strength on the axis. It is obvious that the field strength scales linearly with applied voltage and does not depend on the potentials applied to the quadrupole rods [26], as the axial (z) direction is orthogonal to the x-y plane. Tanner et al. [27] report on stability characteristics of the pressurized quadrupole with auxiliary electrodes and found that the boundaries of stability remain sharply defined for the quadrupole with axial field. Thus the ability of the reaction cell to intercept unwanted ion-molecule reactions by rejection of the precursor ions is retained.

In a common mode of operation, the DRC is pressurized with NH_3 to about P_{NH3} = 20 mTorr (2.7 Pa). For variable hard-sphere (VHS) collisions of Ar^+ with NH_3, the total cross-section is $\sigma_{VHS} = 1/4\ \pi \cdot (d_{NH3} + d_{Ar})^2 = 80$ Å^2, where d_{NH3} and d_{Ar} are VHS molecular diameters [28]. At low energy, the ion-dipole interaction cross-section becomes larger than σ_{VHS}. From σ_{VHS} and P_{NH3}, the minimum average collision number can be estimated as five collisions per 1 cm of cell length. Thus, under these conditions, ions can at most gain about 0.07 eV kinetic energy due to acceleration between collisions (derived from axial field strength of 35 V/m and 0.2 cm mean free path), which is less than the contribution of the rf energy [13]. Although such extra heating (adding about 800 K) does not significantly affect reactivity in most cases (cluster formation may be the only exception), it should dramatically improve ion transit time. For an ion of mass 100 a.m.u. moving at an average kinetic energy of 0.05 eV towards the cell exit, the transit time is expected to be around 300 microsecond, which is of the order of the typical settling time for nonpressurized quadrupoles.

Results and Discussion

Effect of an Axial Field on Pressurized Cell Settling Time and Ion Transit Time

The arrival time distributions for ion pulses of duration of 2 ms introduced into the cell pressurized with Ne at ca. 40 mTorr are shown in Figure 2. Such high pressure is achieved at Ne flow of 3 Ar-equivalent s.c.c.m. which is far greater than the collisional focusing optimum. This high flow was used in order to obtain maximum temporal stretching of the ion pulse. For the same purpose, the cell entrance voltage was set to V_{CE} = 0.

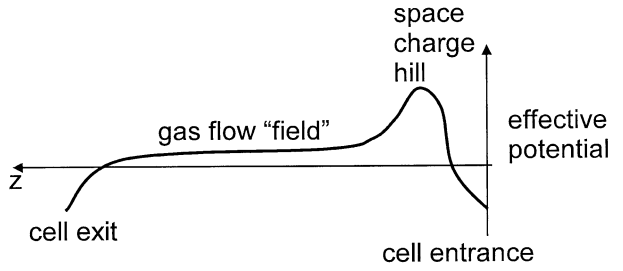

Figure 3. Qualitative model of the axial fields in the cell.

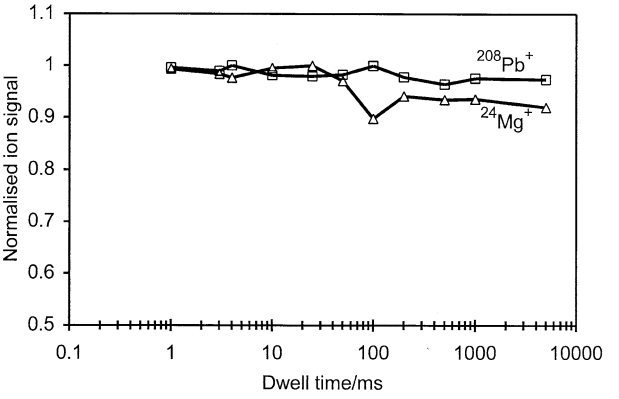

Figure 4. Mg^+ and Pb^+ signals measured sequentially at different dwell time for the cell pressurized with NH_3 at 0.5 Ar-equivalent s.c.c.m. Settling time 3 ms. V_{AFT} = 165 V.

The width of the arrival time distribution of the ion packet passing through the pressurized cell without axial field is increased to 145 ms (f.w.h.m.) by collisions with Ne compared to the 2 ms width of the distribution for a nonpressurized cell. Such broadening can cause temporal homogenization of ion density fluctuations for a quasi-continuous ion beam and has value in high precision isotope ratio measurements, as described in [20]. It also deteriorates the ability of the instrument to respond to very fast transient changes. When V_{AFT} = 50, 100, 150, 250, and 500 V is applied to the auxiliary electrodes, the width of the arrival time distribution is 42.5 ms, 4.9 ms, 4.9 ms, 2.45 ms, and 2.05 ms, respectively. Ion transit time is reduced by as much as a factor of 70. Ion transmission (calculated from the integrated counts for raw data) for a 2 ms transient pulse at an optimum (for transmission) axial field (V_{AFT} = 150 V) is improved 2.2 times compared to V_{AFT} = 0 V.

It is our understanding that the space charge field plays a significant role in the transmission of ions through the cell that is not provided with an axial field. Another mechanism that drags ions through the cell is collisions with the gas that in our configuration is introduced at the entrance of the cell and expands towards the exit aperture, thus having net velocity directed to the exit. A qualitative model of the axial fields in the cell is shown in Figure 3. The ions are accelerated towards the cell by V_{CE} and enter the cell with kinetic energy $KE_0 = eV_{CE} + eV_{IS} + KE_{exp}$, where V_{IS} and KE_{exp} are the potential of the ion source and kinetic energy acquired during the expansion (which depends on ion mass [32]), respectively. As ions move into the cell and collide with the gas molecules, the energy is damped and ions that lose the most tend to stay in the potential well formed at the entrance. This well is gradually filled, and a space charge potential hill develops, with dominant ions defining its characteristics. Ions that retain or gain through multiple collisions enough kinetic energy to overcome this potential hill are pushed by it and by the net gas flow towards the exit, where they are extracted by the field formed by the cell exit aperture biased to V_{CP} (usually −15 to −25 V). The space charge distribution depends on the ion energy, which in turn depends on the origin and the mass of the dominant ions. When the low-mass cut-off is set below *m/z* = 17, for example, for the cell pressurized with ammonia, NH_3^+ is a dominant ion (as the dominant plasma ions transfer charge to NH_3). The space charge then has higher density closer to the entrance of the cell, as the dominant ions are almost stationary. If the bandpass is set to have a high low-mass cut-off, the dominant ion can be, for example, unreacted Ar_2^+ or, if present, a matrix ion derived from the source. As these ions can penetrate deeper into the cell because of their higher kinetic energy, the space charge is distributed differently. Different distributions of the space charge require different times for the steady-state axial fields to establish. When a fast change of the ion density occurs in the cell (for example, an ion pulse is introduced into an "empty" cell, or a change of low-mass cut-off causes ejection of dominant ions), time is needed for the steady-state space charge distribution to be established. As the time required for analyte ions to transit the cell depends on the space charge defined axial field, their observation lags behind the change. Thus, a cell pressurized to a relatively high pressure requires a settling time of many milliseconds for the ion signal to reach a steady state, as observed in [21].

When an additional axial dc-field is provided, the steady-state space charge distribution becomes less dependent on the ion origin or the mass, and ion transport through the cell becomes independent of the space charge distribution. The settling time of the cell after an abrupt change of the ion density is then defined by the time required for the slowest ion to reach the exit, not by the time required to establish the steady-state fields in the cell.

The effect of the applied axial field on the settling time of the cell after a bandpass change is shown in Figure 4. Ion signals for Mg^+ and Pb^+ measured alternatively in one method at q = 0.45 for the cell pressurized with ammonia are observed to be independent of the dwell time (at a settling time of 3 ms). The data were collected on the same instrument as in [21] after its upgrade with the axial field, at V_{AFT} = 165 V. Thus, the axial field allows operation of the instrument with a settling time similar to the settling time of the quadrupole analyzer downstream of the cell.

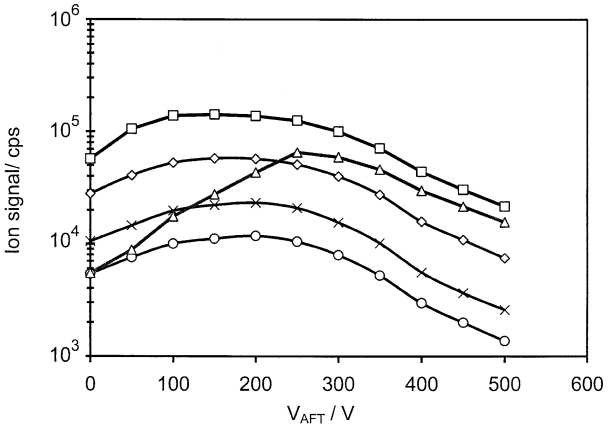

Figure 5. Typical V_{AFT} optimization curves collected at NH_3 flow of 0.5 Ar-equivalent s.c.c.m. for $^{23}Na^+$ (shown as crosses), $^{24}Mg^+$ (circles), $^{39}K^+$ (diamonds), $^{40}Ca^+$ (squares), $^{56}Fe^+$ (triangles).

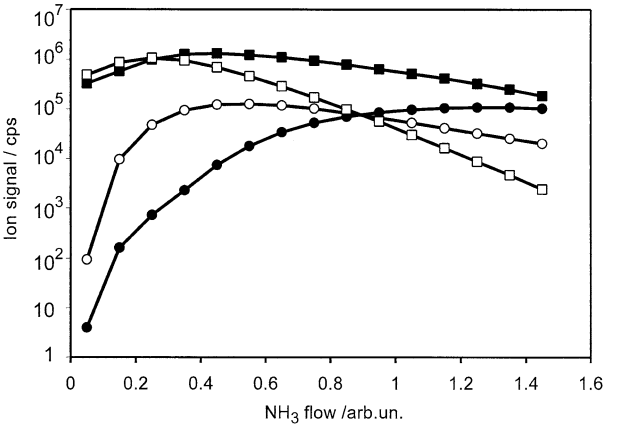

Figure 6. Fe^+ (squares) and $Fe^+(NH_3)_2$ (circles) signals for V_{AFT} = 0 (open markers) and V_{AFT} = 275V (solid markers) as functions of NH_3 flow.

Effect of Axial Field on Cluster Formation and Reactive Analyte Loss

It is to be noted that the V_{AFT} at which the transmission maximizes depends on several factors that include cell gas pressure, ratio of ion and gas masses, reactivity of the ion towards the gas or its impurities, and the amplitude of the rf voltage applied to the quadrupole (V_{rf} = 130 V peak-to-peak for the data shown in the previous section). Figure 5 gives an example of the axial field optimization for Na^+, Mg^+, K^+, Ca^+, and Fe^+ at typical DRC conditions (NH_3 flow of 0.5, $V_{CE} = V_{CP} = -17$ V, V_{rf} = 200 V peak-to-peak). Signals for the ions that form metal-ammonia clusters were found to maximize at higher V_{AFT} than those for nonreactive ions. Fe^+ is reported to cluster with ammonia forming $Fe^+(NH_3)_n$, n = 1–3, with the total rate of clustering of $(1.7 \pm 0.5) \times 10^{-11}$ cm^3 molecule^{-1} s^{-1} at 0.35 torr He buffer [29]. These clustering reactions can be readily observed in the DRC if the mass bandpass is set to a value allowing stability of both the measured cluster and its precursor (Fe^+) in the quadrupolar field. Figure 6 shows the profiles of the clustering reactions measured at q = 0.2 (wide bandpass). With NH_3 flow (0.5 Ar-equiv, s.c.c.m.) set to completely suppress ArO^+ interference on Fe^+, the n = 2, 3 clusters are significantly suppressed by an applied axial field, and Fe^+ scattering and reactive losses (ca. $10^{-2.8}$ per unit flow) are significantly reduced (to ca. 10^{-1} per unit flow). We attribute these observations to the fact that the rate of clustering reactions, which are usually tri-molecular processes (a third molecule or a second collision is required to stabilize the cluster by removing the excess energy that otherwise would cause dissociation), is very sensitive to ion kinetic energy and thus is reduced even by small ion heating by the axial field. Typical spectra for a solution containing Co, Rb, Rh, and Cs are shown in Figure 7. Spectra were collected at a wide bandpass (q = 0.3) to ensure that the metal ions that are the precursors for the clusters are stable in the quadrupolar field (Figure 7a and b). Rh^+ and Co^+ form $M^+ \cdot (NH_3)_n$ with n = 1–4, for which (at NH_3 flow of 0.5) the most abundant species are $Rh^+ \cdot (NH_3)_2$, $Co^+ \cdot (NH_3)_2$, and

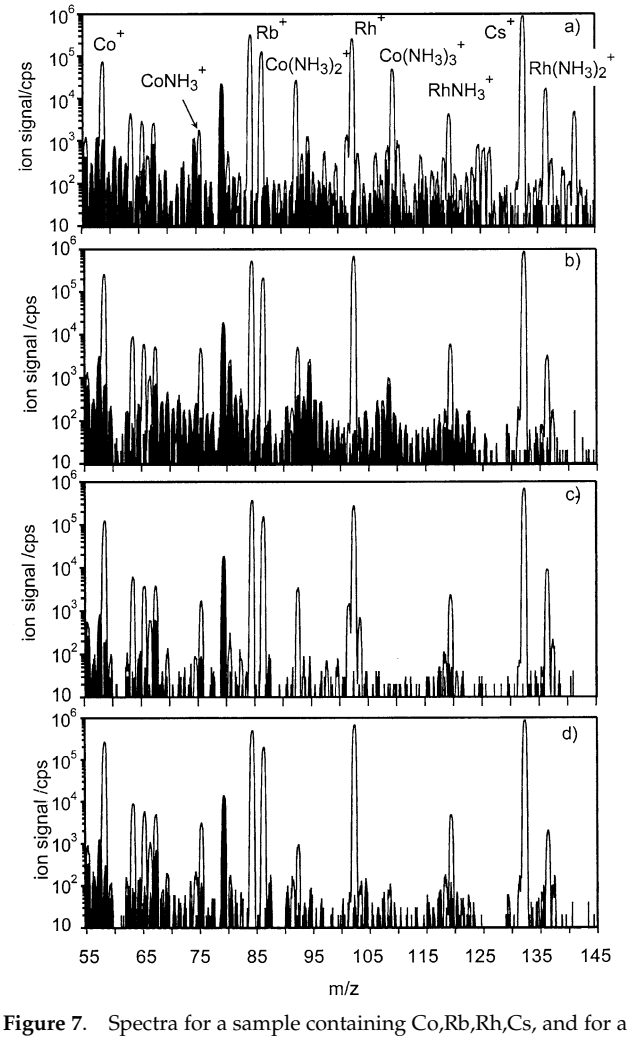

Figure 7. Spectra for a sample containing Co,Rb,Rh,Cs, and for a blank (black) collected with NH_3 flow of 0.5 Ar-equivalent s.c.c.m. at: (**a**) q = 0.3, V_{AFT} = 0; (**b**) q = 0.3, V_{AFT} = 300V; (**c**) q = 0.5, V_{AFT} = 0; (**d**) q = 0.5, V_{AFT} = 300V.

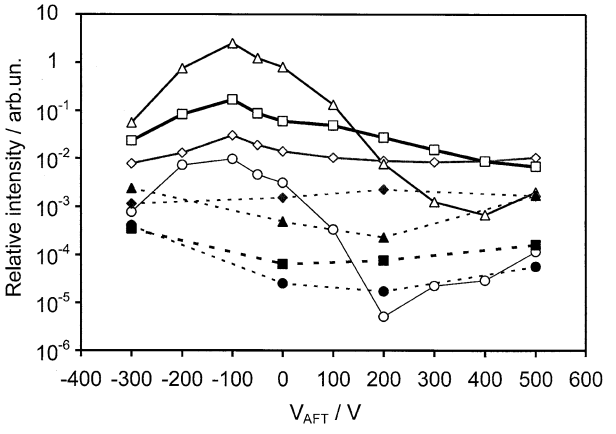

Figure 8. Relative intensity for nickel-ammonia clusters as a function of axial field strength. Shown are the ratios Ni^+NH_3/Ni^+ (diamonds), $Ni^+(NH_3)_2/Ni^+$ (triangles), $Ni^+(NH_3)_3/Ni^+$ (squares), $Ni^+(NH_3)_4/Ni^+$ (circles), at q = 0.2 (open markers) and q = 0.6 (solid markers).

$Co^+ \cdot (NH_3)_3$. Rb^+ and Cs^+ do not form clusters with ammonia to a significant extent. It can be seen that at V_{AFT} = 300 V, signals for nonreacting Rb^+ and Cs^+ are increased by a factor of 1.6 and 1.0 while for Co^+ and Rh^+ the factors are 3.5 and 2.6, respectively. With the axial field $Rh^+ \cdot (NH_3)_2$, $Co^+ \cdot (NH_3)_2$, and $Co^+ \cdot (NH_3)_3$ are suppressed 5.2, 9.3, and 326 times, respectively. The field does not significantly affect the rate of formation of the first clusters.

The axial field is not as efficient at interception of the formation of unwanted ions (including cluster ions) as the fast rejection of the precursors because of their instability in the quadrupolar field. Spectra for the same sample collected at q = 0.5 with and without axial field are shown in Figure 7c and d. When $Co^+ \cdot (NH_3)_3$ (*m/z* = 110) is measured at q = 0.5, its primary precursor ion (Co^+) experiences a field with corresponding stability parameter q^+_{Co} = 0.93 and is outside of the boundaries of stability (q = 0.909 at a = 0). The cluster is then suppressed 3×10^3 times compared to that measured at q = 0.3 (q^+_{Co} = 0.56), i.e., about one order of magnitude higher suppression than that achieved by the axial field alone. The axial field, however, can mitigate the effect of analyte loss to cluster formation by reducing the rate of cluster formation. When it is necessary to use a wide bandpass (for example, to promote atom transfer or to use clustering reaction products as analyte ions), the axial field can provide an additional means for controlling cluster formation. Nickel-ammonia cluster signals as a function of V_{AFT} for q = 0.2 and q = 0.6 are shown in Figure 8. At q = 0.2, the axial field hardly affects formation of the first cluster while it suppresses the n = 2, 3, 4 clusters by up to 9, 1200, and >610 (background limited) times, respectively. At q = 0.6 and zero axial field, n = 1–4 clusters are suppressed 9, 950, 1650, and >120 (background limited) times, respectively, relative to q = 0.25.

In-Cell Energy Discrimination with Retarding Axial Field

Figure 8 shows that cluster formation maximizes near V_{AFT} = −100 V, which is an expected effect of slowing the ions in a retarding axial field. At more negative voltage, somewhat surprisingly, the signals for the clusters are suppressed more than for Ni^+. We attribute this to a differential energy discrimination against lower energy ions by the retarding field provided inside the cell. As the rate of cluster formation is very sensitive to the ion energy, only the slowest fraction of Ni^+ ions reacts to form clusters. Now, let us consider two Ni^+ ions that collide with NH_3, one of which is slower and forms the cluster (in fact, participation of another NH_3 molecule is required for Ni^+NH_3 to be stable), and another which is faster and thus does not react. The product cluster ions will most likely on average be less energetic than the unreacted Ni^+ ion. Subsequent collisions will cause this difference in kinetic energy to diminish and, if there are enough collisions, the energy distributions of the cluster ion population and unreacted ion population can become similar and close to the thermal distribution. If a continuously retarding field is provided, less energetic cluster ions will be decelerated and ultimately scattered before the energy distributions overlap. Similarly, the products of two first cluster ions colliding with an NH_3 molecule, one forming a cluster and the other not, will be retarded by the field differently because of a difference in the energy after the collision. Also, a higher order cluster can distribute the collision energy into more internal degrees of freedom, securing the energy difference. It can be speculated that first order clusters are discriminated less by the retarding field than the higher order clusters (see Figure 8) because of the dependence of the cluster kinetic energy on the order of the cluster and the number of degrees of freedom.

$^{127}IH_2^+$ Suppression by In-Cell Energy Discrimination for Improving $^{129}I^+$ Detection

One could apply similar considerations to polyatomic ion formation in the cell. Slower atomic ions have, first, higher collision cross-section (a good estimate of which is the Langevin cross-section that is inversely proportional to velocity [30]). Note that the ion size for slower ions does not define the collision cross-section, especially in collisions with molecules that have high polarizability or permanent dipole moment, as the ion-dipole interactions are dominant at low speed. Second, slower ions have higher reaction cross-section [31]. Being produced from the lower energy fraction of precursor ions, polyatomic ions should have average velocity that is lower than the velocity of unreacted precursor ions. This in turn should cause the collision cross-section to be higher for polyatomic ions and thus more energy damping collisions should occur for product ions. If the number of collisions is high enough, both precursor and

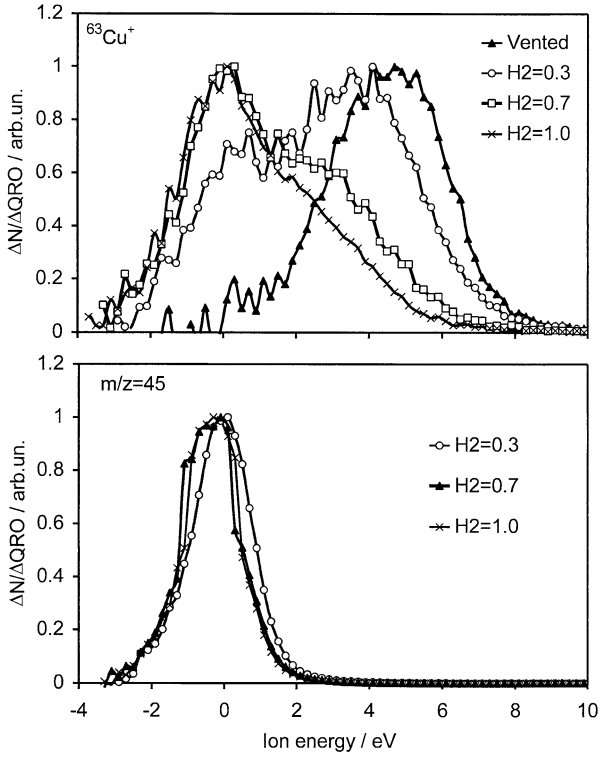

Figure 9. Post-cell energy distributions of in-plasma produced $^{63}Cu^+$ ions (**a**) and in-cell produced ions at $m/z = 45$ (**b**) at different H_2 flows.

product ion populations will equilibrate with the gas temperature, and their energy distributions upon exiting the cell will be indistinguishable. Figure 9 provides measured energy distributions of the ions (both derived from the source and produced within the cell) downstream of the cell as a function of H_2 gas flow. These energy distributions were obtained by differentiating the ion signal as a function of a stopping potential applied to a quadrupole analyzer in the manner similar to that described in [32]. Ions at $m/z = 45$ are produced in the cell (as evidenced by dramatic increase in intensity with gas flow; isotope pattern is close to that of $C_2H_5O^+$). The energy distributions of these are relatively narrow and are centered close to 0 eV at all H_2 flows. The energy distributions of plasma-produced Cu^+ ions from the sample are wider, and when no gas is introduced into the cell, are centered about 5 eV. At a low flow, a fraction of the ions is cooled by collisions, and the energy distribution is bimodal. At higher flow, a higher fraction of ions are cooled and the energy distribution is centered close to 0 eV. Setting an energy barrier at, for example, 1.5 eV downstream of the cell will suppress most of the ions at $m/z = 45$. At H_2 flows of 0.3, 0.7, 1.0 (corresponding to 0.21, 0.49, and 0.7 s.c.c.m., respectively), the fractions of interference ions that penetrate the barrier and may be detected, when calculated by integrating the plots in Figure 9b, are 3.4, 2.2, and 1.9%, respectively. Similar calculations for the fractions of Cu^+ ions that may be detected, give 68, 42, and 33%, respectively, of the total integral.

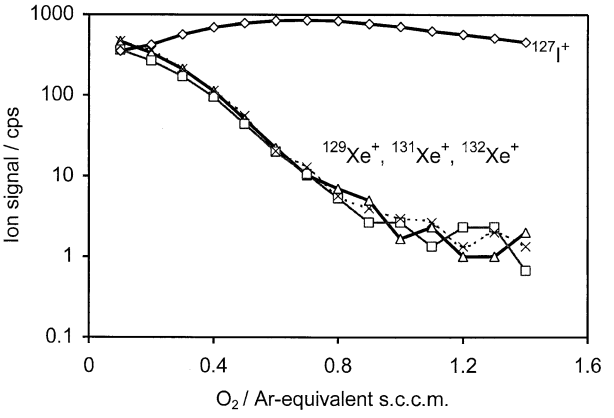

Figure 10. Profiles for I^+ and Xe^+ reaction with O_2.

To achieve three orders of magnitude suppression of ions at $m/z = 45$, the energy barrier must be set at 4.5 eV, 4.1 eV, and 3.9 eV at the stated flows, respectively. The resultant transmission efficiency for Cu^+ ions of 21.5, 10.8, and 7.4%, respectively, can be achieved. Thus, high suppression of in-cell formed ions by post-cell energy discrimination is necessarily accompanied by significant suppression of analyte ion signals.

Application of an in-cell continuous retarding field can potentially decelerate and scatter slower polyatomic ions before the energies of the analyte ions are equilibrated by collisions to being indistinguishable from those of the in-cell produced ions. This potentially should give better differential suppression of the in-cell produced polyatomics.

One of the important cases where energy discrimination can provide significant benefits is suppression of hydride ions produced in the cell, as pressurized quadrupoles usually operate at a relatively low resolution (with a bandpass of about 5–10 a.m.u.) and cannot efficiently suppress hydride ion precursors without affecting analyte ions that differ in mass by only 1 or 2 a.m.u.

We compared the efficiency of in-cell continuous energy discrimination versus that of post-cell discrete energy discrimination while studying the charge-exchange reaction of $^{129}Xe^+$ with O_2 for the purpose of determination of isobaric $^{129}I^+$. Use of oxygen for suppressing $^{129}Xe^+$ in ICP-MS was first reported by Eiden and co-workers [33]. The rate constant for charge exchange is relatively high ($k_r = 1.1 \times 10^{-10}$ molecule^{-1} s^{-1} cm^3 [34]) and the reaction proceeds relatively fast in the DRC (Figure 10), removing $^{129}Xe^+$ by more than two orders of magnitude at 0.5 s.c.c.m. of O_2 flow (0.7 Ar-equivalent s.c.c.m.). At the same time, $^{127}I^+$ is virtually nonreactive with O_2 and is focused by collisions so that the signal is increased ca. three times at O_2 flow of 0.5 s.c.c.m. when $V_{AFT} = 275$ V. The purity of O_2 is very important, as I^+ can be lost through reactions with impurities [Dr. Katsu Kawabata, Perkin-Elmer Instruments, personal communication].

Control of impurities is very important also because

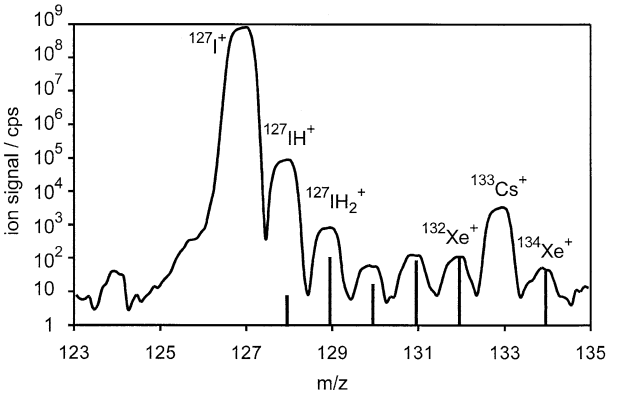

Figure 11. Mass-spectrum for a sample containing I_2 (10 ppm) and Cs (100 ppt) measured at O_2 flow of 0.4 Ar-equivalent s.c.c.m. and no energy discrimination. Vertical lines show isotope pattern of Xe.

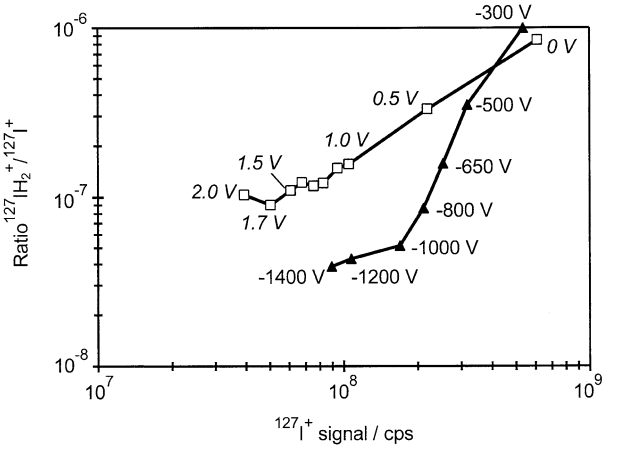

Figure 12. Relative abundance of a new interference IH_2^+ plotted against I^+ signal for different post-cell energy barriers (open squares) and in-cell retarding field strength (filled triangles). The heights of the potential barrier downstream the cell (*in italic font*); the applied to the auxiliary electrodes potential are shown next to corresponding points on the graph.

of the high demands on the abundance ratio of $^{129}I/^{127}I$, which is of interest for environmental or nuclear waste monitoring. In such cases, the formation of trace amounts of $^{127}IH_2^+$ can become critical. A typical mass spectrum obtained for 10 ppm I_2 solution in 1% isopropyl alcohol is shown in Figure 11. At an intermediate flow of oxygen of 0.4 Ar-equivalent s.c.c.m., $^{129}Xe^+$ is suppressed to about 100 cps (as can be seen from signals for other Xe isotopes and isotopic abundance of $^{129}Xe^+$). However, a new interference ($^{127}IH_2^+$) is formed at a level of about 1000 cps. Compared to the standard (cell vented) mode, the $^{127}IH_2^+/^{127}I^+$ ratio increases from $<2.5 \times 10^{-7}$ to 9×10^{-7} at O_2 flow of 0.4 and to 4.9×10^{-6} at O_2 flow of 1.3 Ar-equivalent s.c.c.m. Calculated reaction enthalpies for several possible impurities (H_2, H_2O, NH_3, H_2O_2, CH_2O, CH_3OH, C_2H_5OH, C_3H_7OH, C_3H_6O, CH_4, C_2H_4, C_2H_6) using data from [35] show exothermic channels $I^+ + XH_2 \rightarrow IH_2^+ + X$ for hydrogen, hydrogen peroxide, formaldehyde, methanol, ethanol, propanol, and ethane. It is conceivable that some of these impurities can be present in the cell gas at the 0.001% level. It is also possible that $^{127}IH_2^+$ is formed in the cell by an H-atom transfer reaction between $^{127}IH^+$ (produced in the plasma at a level of about 0.01%, estimated with the use of thermochemical data [35] bond strength of ca. 3.2 eV) and an unknown impurity in the cell gas; however, we could not determine an impurity molecule for which the reaction would be exothermic.

As a result of the reactions with impurities, when maximum suppression of plasma produced $^{129}Xe^+$ interference is achieved, new interference is formed at a significant level. While we introduced the purest available gas through an oxygen purifier and used an all stainless steel gas manifold system, it is clear that even the most exquisite control of gas purity will be challenged to prevent the formation of product ions that are at 10^{-6} level of the precursor. Using a narrow mass bandpass to reject the $^{127}I^+$ precursor is not efficient, especially at a high gas flow, as unit mass resolution is not achievable in the high-pressure quadrupole without significant compromise in transmission.

We have also tried using C_2H_6 for charge exchange with $^{129}Xe^+$, as the ionization potential of ethane is lower than that of Xe (11.52 eV versus 12.13 eV) but higher than that of I (10.451 eV). Reaction with Xe^+ appeared to proceed, however, severe IH_2^+ formation increased the background at m/z =129 and caused loss of I^+. Quantitative conversion of all the iodine ions into IH_2^+ to be used as analytes, in which case hydride interferences would not be a problem, was unsuccessful due to the slow kinetics of the reaction.

Another method of suppressing secondary interferences is energy discrimination. It can be enacted post-cell [36] or, as discussed in the previous section, in-cell by providing a continuous retarding axial field. We investigated both methods for suppression of the IH_2^+ interference. In order to minimize the H-atom transfer reaction and to reduce the amount of in-plasma produced IH_2^+, we introduced I_2 as a vapour by placing iodine flakes into a dried cyclonic spray chamber (and using its drain port for Ar gas flow, with nebulizer port blocked). In this manner, the $^{127}IH^+/^{127}I^+$ ratio in standard mode dropped to 5.4×10^{-7}, implying that $^{127}IH_2^+/^{127}I^+$ must be vanishingly small in the plasma when a completely dry sample is introduced.

Figure 12 shows the suppression of $^{127}IH_2^+$ achieved either by biasing the analyzing quadrupole to a potential V_{QRO} higher than the DC bias of the cell V_{CRO} (post-cell discrimination), or by applying a negative voltage V_{AFT} to the auxiliary electrodes to provide a retarding axial field (in-cell discrimination). When applying post-cell discrimination, V_{CRO} = +0.5 V and V_{AFT} = 0 were used while V_{QRO} was varied to obtain the desired energy barrier. For in-cell discrimination, V_{CRO} = +0.5 V and V_{QRO} = –5 V were used while V_{AFT} was varied to obtain the desired retarding field. In-cell

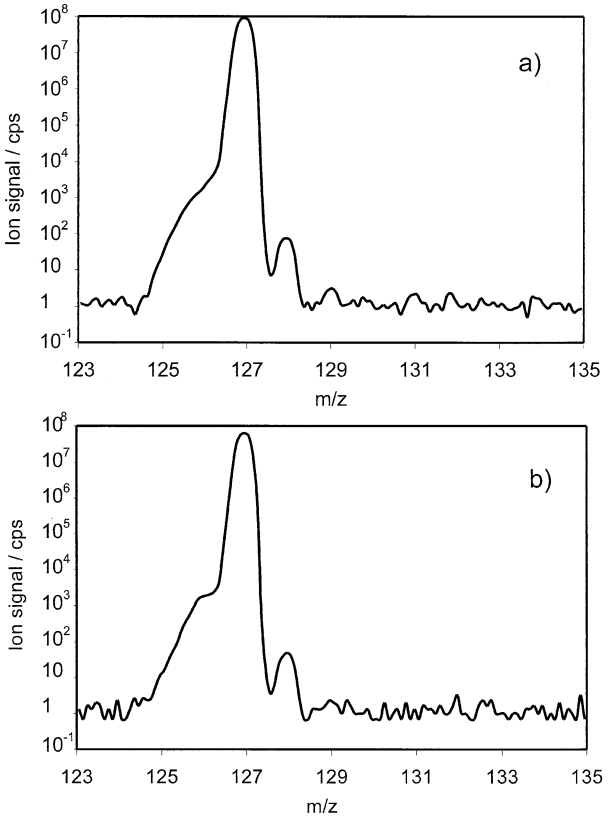

Figure 13. Mass spectra for iodine sample introduced as a vapor and collected at different in-cell retarding field strength (**a**) V_{AFT} = −1400 V, V_{QRO} = −5 V; (**b**) V_{AFT} = −500 V, V_{QRO} = −0.6 V.

discrimination causes less suppression of the analyte ($^{127}I^+$, horizontal axis) for the same suppression of the interference. With the retarding potential at V_{AFT} = −1400 V, the background at m/z = 129 was 4 cps while ca. 1×10^8 cps of $^{127}I^+$ signal was retained. The mass spectra collected with the retarding axial field are shown in Figure 13. At V_{AFT} = −1400 V, the ratio of background at m/z = 129 to $^{127}I^+$ signal is 3.3×10^{-8}. A similar background-to-analyte ratio (3.5×10^{-8}) could be obtained at V_{AFT} = −500 V when V_{QRO} = −0.6 V was used, at about 40% lower signal for $^{127}I^+$. About 30–50% of the background appears to be due to residual $^{129}Xe^+$.

Assuming Poisson distribution of the background at m/z = 129, the 3σ 10 s detection limit can be estimated as ca. 2×10^{-8} (in units of $^{127}I^+$ signal). Thus, it should be possible to detect ^{129}I in the presence of 10^7 times higher abundance of ^{127}I when reaction with O_2 is used for $^{129}Xe^+$ suppression and in-cell energy discrimination is used for $^{127}IH_2^+$ suppression. Use of dry plasma conditions is preferred to prevent formation of hydrides in the plasma (which are less amendable to energy discrimination at the required levels).

Conclusions

Use of an in-cell dc-axial field improves the ability of the quadrupole reaction cell to quickly respond to fast transient changes in ion beam density or mass bandpass conditions. The field reduces the settling time of the pressurized quadrupole to the values similar to those of the typical quadrupole mass analyzers operated under collision-less conditions (to <4 ms). It also improves the transmission of analyte ions. It suppresses formation of higher order clusters (n = 2–4) by one to three orders of magnitude under wide (low q) bandpass conditions. Narrowing the bandpass to the value at which the cluster precursor is unstable in the quadrupole field, however, is a complementary and more efficient way of suppressing cluster formation than the axial field on its own. Compromise field strength can be used at which clusters are suppressed, fast settling time is achieved, and transmission of most analytes measured in pressurized mode is close to optimal.

A retarding axial field can be used for in situ energy discrimination against cluster and polyatomic ions formed in the cell. In-cell energy discrimination can become a preferential way of suppression of the in-cell formed polyatomic ions that differ in mass by only a few a.m.u. from the analyte ions, such as the case of hydride ions. Compared to post-cell potential energy discrimination enacted using an energy barrier downstream of the cell, in-cell energy discrimination can provide higher discrimination efficiency. This has been shown by example of the suppression of $^{127}IH_2^+$ formed (presumably from gas impurities) in the cell pressurized with O_2 for suppression of Xe^+. In this case in-cell energy discrimination of $^{127}IH_2^+$ by the retarding axial field is shown to reduce the abundance of the background at m/z = 129 to ca. 3×10^{-8} of the $^{127}I^+$ signal.

Chemical resolution of $^{129}I^+/^{129}Xe^+$ isobars with simultaneous suppression of in-cell formed $^{127}IH_2^+$ can become an important application of the DRC when it is desired to measure low levels of $^{129}I^+$ in the presence of high abundance of $^{127}I^+$.

Conceivably, additional control of the cluster and polyatomic ion formation and transmission provided by the axial field can be useful when such ions are used for analyte detection.

Acknowledgments

The authors thank Alexander Loboda (MDS SCIEX) for useful discussions of the axial field geometry, Ed Masionis (MDS SCIEX) for designing the prototypes of the axial field cell, and Katsu Kawabata (Perkin-Elmer Instruments) for his insight into practical challenges of $^{129}I^+$ detection.

References

1. Bandura, D. R.; Baranov, V. I.; Tanner, S. D. *Anal. Chem.* **2002**, *74,* 1497–1502.
2. Boulyga, S. F.; Dietze, H. J.; Becker, J. S. *Mikrochim. Acta* **2001**, *137,* 93–103.
3. Boulyga, S. F.; Becker, J. S. *Fresenius J. Anal. Chem.* **2001**, *370,* 618–623.
4. Chang, Y. L.; Jiang, S. J. *J. Anal. Atom. Spectrom.* **2001**, *16,* 1434–1438.

5. Gunther, D.; Hattendorf, B.; Audetat, A. *J. Anal. Atom. Spectrom.* **2001**, *16,* 1085–1090.
6. Hattendorf, B.; Gunther, D.; Schonbachler, M.; Halliday, A. *Anal. Chem.* **2001**, *73,* 5494–5498.
7. Ingle, C. P.; Appelblad, P. K.; Dexter, M. A.; Reid, E. J.; Sharp, B. L. *J. Anal. Atom. Spectrom.* **2001**, *16,* 1076–1084.
8. Latino, J.; Neubauer, K.; Wolf, R. E.; Wallace, G.; Thomsen, M. *At. Spectrosc.* **2001**, *22,* 306–311.
9. Leach, A. M.; Hieftje, G. M. *Int. J. Mass Spectrom.* **2001**, *212,* 49–63.
10. Marchante Gayon, J. M.; Feldmann, I.; Thomas, C.; Jakubowski, N. *J. Anal. Atom. Spectrom.* **2001**, *16,* 457–463.
11. Simpson, L. A.; Thomsen, M.; Alloway, B. J.; Parker, A. *J. Anal. Atom. Spectrom.* **2001**, *16,* 1375–1380.
12. Tanner, S. D.; Baranov, V. I. *J. Am. Soc. Mass Spectrom.* **1999**, *10,* 1083–1094.
13. Baranov, V. I.; Tanner, S. D. *J. Anal. Atom. Spectrom.* **1999**, *14,* 1133–1142.
14. Tanner, S. D.; Baranov, V. I. *At. Spectrosc.* **1999**, *20,* 45–46.
15. Tanner, S. D.; Baranov, V. I.; Vollkopf, U. *J. Anal. Atom. Spectrom.* **2000**, *15,* 1261–1269.
16. Vollkopf, U.; Klemm, K.; Pfluger, M. *At. Spectrosc.* **1999**, *20,* 53–59.
17. Bandura, D. R.; Baranov, V. I.; Tanner, S. D. *Fresenius J. Anal. Chem.* **2001**, *370,* 454–470.
18. Moens, L. J.; Vanhaecke, F. F.; Bandura, D. R.; Baranov, V. I.; Tanner, S. D. *J. Anal. Atom. Spectrom.* **2001**, *16,* 991–994.
19. Douglas, D. J.; French, J. B. *J. Am. Soc. Mass Spectrom.* **1992**, *3,* 398–408.
20. Bandura, D. R.; Baranov, V. I.; Tanner, S. D. *J. Anal. Atom. Spectrom.* **2000**, *15,* 921–928.
21. Hattendorf, B.; Gunther, D. *J. Anal. Atom. Spectrom.* **2000**, *15,* 1125–1131.
22. Morris, M.; Thibault, P.; Boyd, R. K. *J. Am. Soc. Mass Spectrom.* **1994**, *5,* 1042–1063.
23. Thomson, B. A.; Jolliffe, C. L. Spectrometer with Axial Field. U.S. Patent 5,847,386, **1998**.
24. Lock, C. M.; Dyer, E. *Rapid Commun. Mass Spectrom.* **1999**, *13,* 432–448.
25. Loboda, A.; Krutchinsky, A.; Loboda, O.; McNabb, J.; Spicer, V.; Ens, W.; Standing, K. *Eur. J. Mass Spectrom.* **2000**, *6,* 531–536.
26. Gerlich, D. *Advanced Chemical Physics Series.* 1992, LXXXII. John Wiley and Sons: pp 1–176.
27. Tanner, S. D.; Baranov, V. I.; Bandura, D. R. *Spectrochim. Acta Reviews*, unpublished.
28. Bird, G. A. *Molecular Gas Dynamics and the Direct Simulation of Gas Flows.* Oxford University Press Inc: New York, 1995; p 409.
29. Milburn, R. K.; Baranov, V. I.; Hopkinson, A. C.; Bohme, D. K. *J. Phys. Chem. A* **1998**, *102,* 9803–9810.
30. Hasted, J. B. Physics of Atomic Collisions. Butterworth and Co: London, 1964; p 478.
31. Ervin, K. M.; Armentrout, P. B. *J. Chem. Phys.* **1985**, *83,* 166–189.
32. Fulford, J. E.; Douglas, D. J. *Appl. Spectrosc.* **1986**, *40,* 971–974.
33. Eiden, G. C.; Barrinaga, C. J.; Koppenaal, D. W. *Rapid Commun. Mass Spectrom.* **1997**, *11,* 37–42.
34. Anicich, V. G. Ion Reactions Databases. *Astrophys. J. Supp. Series* **1993**, *84,* 215. Also, http://astrochem.jpl.nasa.gov/asch/.
35. Lias, S. G.; Bartmess, J. E.; Liebman, J. F.; Holmes, J. L.; Levin, R. D.; Mallard, W.G. *J. Phys. Chem. Ref. Data* **1988**, *17(Suppl. 1).*
36. Rowan, J. T.; Houk, R. S. *Appl. Spectrosc.* **1989**, *43,* 976–980.
37. MKS Instruments, Methuen, MA. http://www.mksinstruments.com/pdf/146Cman.pdf.